The Meteoritical Society

Meteoritics & Planetary Science 51, Nr 12, 2274–2292 (2016)
doi: 10.1111/maps.12716

Hyperspectral mapping of alteration assemblages within a hydrothermal vug at the Haughton impact structure, Canada

Rebecca N. GREENBERGER[1,9,*], John F. MUSTARD[1], Gordon R. OSINSKI[2,3,4], Livio L. TORNABENE[2,3,5], Alexandra J. PONTEFRACT[2,3,6], Cassandra L. MARION[2,3], Roberta L. FLEMMING[2,3], Janette H. WILSON[7], and Edward A. CLOUTIS[8]

[1]Department of Earth, Environmental, and Planetary Sciences, Brown University, 324 Brook St, Box 1846, Providence, Rhode Island 02912, USA
[2]Centre for Planetary Science and Exploration, University of Western Ontario, 1151 Richmond Street, London, Ontario N6A 5B7, Canada
[3]Department of Earth Sciences, University of Western Ontario, 1151 Richmond Street, London, Ontario N6A 5B7, Canada
[4]Department of Physics and Astronomy, University of Western Ontario, 1151 Richmond Street, London, Ontario N6A 5B7, Canada
[5]SETI Institute, 189 Bernardo Ave, Mountain View, California 94043, USA
[6]Planetary Science Institute, 1700 East Fort Lowell, Suite 106, Tucson, Arizona 85719, USA
[7]Headwall Photonics, Inc., 601 River Street, Fitchburg, Massachusetts 01420, USA
[8]Department of Geography, University of Winnipeg, 515 Portage Avenue, Winnipeg, Manitoba R3B 2E9, Canada
[9]Present address: Jet Propulsion Laboratory, California Institute of Technology, 4800 Oak Grove Drive, M/S 171-310, Pasadena, California 91109, USA
[*]Corresponding author. E-mail: rebecca.n.greenberger@jpl.nasa.gov

(Received 30 March 2015; revision accepted 12 July 2016)

Abstract–Meteorite impacts on Earth and Mars can generate hydrothermal systems that alter the primary mineralogies of rocks and provide suitable environments for microbial colonization. We investigate a calcite–marcasite-bearing vug at the ~23 km diameter Haughton impact structure, Devon Island, Nunavut, Canada, using imaging spectroscopy of the outcrop in the field (0.65–1.1 μm) and samples in the laboratory (0.4–2.5 μm), point spectroscopy (0.35–2.5 μm), major element chemistry, and X-ray diffraction analyses. The mineral assemblages mapped at the outcrop include marcasite; marcasite with minor gypsum and jarosite; fibroferrite and copiapite with minor gypsum and melanterite; gypsum, Fe^{3+} oxides, and jarosite; and calcite, gypsum, clay, microcline, and quartz. Hyperspectral mapping of alteration phases shows spatial patterns that illuminate changes in alteration conditions and formation of specific mineral phases. Marcasite formed from the postimpact hydrothermal system under reducing conditions, while subsequent weathering oxidized the marcasite at low temperatures and water/rock ratios. The acidic fluids resulting from the oxidation collected on flat-lying portions of the outcrop, precipitating fibroferrite + copiapite. That assemblage then likely dissolved, and the changing chemistry and pH resulting from interaction with the calcite-rich host rock formed gypsum-bearing red coatings. These results have implications for understanding water–rock interactions and habitabilities at this site and on Mars.

INTRODUCTION

The heat resulting from impact processes generates hydrothermal systems when water or ice is present in the target rocks (e.g., Newsom 1980; Naumov 2005; Osinski et al. 2013). Evidence of hydrothermal systems is seen at most complex craters on Earth that have been studied in any detail, with hydrothermal mineralization identified in impact melt-bearing units, the central uplift, ejecta, the crater rim, and sediments from lakes filling the craters (Osinski et al. 2013). There is reported postimpact hydrothermal alteration at structures as

small as Lonar crater (1.8 km diameter; Hagerty and Newsom 2003). A range of secondary minerals have been identified at terrestrial impact structures, including silicates (clays, zeolites, feldspars, quartz), carbonates, sulfides, sulfates, native elements, oxides/hydroxides, and halides (Naumov 2005; Osinski et al. 2013), and models have placed constraints on the mineral assemblages expected through similar processes on Mars (Schwenzer and Kring 2009, 2013; Schwenzer et al. 2012).

Key to understanding these impact-generated hydrothermal systems are the mineral assemblages that form through low-temperature weathering of original hydrothermal mineralization after hydrothermal circulation ceased because these are the assemblages observed today (Izawa et al. 2011; Osinski et al. 2013). Both the hydrothermal mineralization and the weathering products elucidate the conditions of water–rock interactions since the impact event and shed light on environments that are promising for microbial colonization (Newsom et al. 1996, 2001; Kring 2000; Abramov and Kring 2005; Schulze-Makuch et al. 2007; Parnell et al. 2010; Izawa et al. 2011; Osinski et al. 2013; Sapers et al. 2014). Furthermore, studies of aqueous processes within terrestrial impact structures can aid in our understanding of similar processes on Mars, where such systems likely occurred (e.g., Newsom 1980; Newsom et al. 2001; Osinski et al. 2013; Tornabene et al. 2013).

Specific morphologies and special characteristics on Mars have been attributed to impact-driven hydrothermal systems, such as at Toro crater (Marzo et al. 2010) and Holden crater (Tornabene et al. 2009; Osinski et al. 2013), and secondary minerals throughout highly cratered regions of Mars have been suggested to form from a variety of impact-induced alteration pathways, including hydrothermal systems (Tornabene et al. 2013). In situ evidence from the Opportunity rover includes Ca-sulfate veins and deposits enriched in Zn that may have formed from impact-driven hydrothermal processes at the ~22 km diameter Endeavour Crater (Squyres et al. 2012; Arvidson et al. 2014).

Studies of mineral deposits formed through impact-generated hydrothermal processes on Earth using remote sensing technologies can help us to better understand such systems and lead to development of exploration criteria for investigating similar deposits on Mars. Here, we investigate a vug lined with hydrothermal calcite and marcasite formed through impact processes at the Haughton impact structure, Devon Island, Nunavut, Canada, using novel techniques. Previous work by Izawa et al. (2011) characterized individual samples from the vug and the habitability of the weathering products, and their work suggested that the marcasite altered and weathered at low temperatures to sulfates and oxides. What remains unexamined is the spatial relationships between the different mineral assemblages, which provide new insights into the water–rock interactions and habitability of this site. We expand on work by Izawa et al. (2011) by using imaging spectroscopy in the field and laboratory to map the spatial distributions of the primary hydrothermal mineralization and later low-temperature weathering products. We report the results of spectral mapping of the deposit; the insights into the evolution of fluids as temperatures, redox states, and chemistries changed; and the implications for detecting and understanding the habitability of such systems on Mars.

GEOLOGICAL SETTING

The calcite–marcasite-bearing vug within the Haughton impact structure is located in the High Arctic of Canada at UTM 16N 0428046 E, 8364683 N (Fig. 1). The Haughton impact structure has a ~23 km apparent diameter (Osinski et al. 2005b) and is dated to 23.5 ± 2.0 Ma (Young et al. 2013). This complex impact structure formed from a meteorite impact into ~1880 m of Lower Paleozoic sedimentary rocks and the underlying Precambrian crystalline basement rocks (Osinski et al. 2005b). The clast-rich impact melt sheet originally covered an area approximately 12 km in diameter (125 km^2) and today covers ~54 km^2 of the crater interior (Osinski et al. 2005b), containing lithic clasts within a matrix of quenched calcite melt, silicate glass, and anhydrite (Osinski and Spray 2001, 2003; Osinski et al. 2005b). The geologic units at the impact structure have been mapped on the ground through traditional geologic methods by Osinski et al. (2005b), and these units are in excellent agreement with lithologic mapping using orbital spectroscopic remote sensing data by Tornabene et al. (2005).

There is evidence for structurally controlled hydrothermal mineralization throughout the Haughton impact structure, with hydrothermal mineralization identified in the impact melt rocks, central uplift, and faulted crater rim (Osinski et al. 2001, 2005a). Minerals that formed in these hydrothermal systems include calcite, selenite, marcasite, quartz, celestite, barite, fluorite, and Fe oxides/hydroxides (Osinski et al. 2005a). We focus here on the largest single hydrothermal deposit at Haughton, a calcite- and marcasite-bearing vug within the impact melt rocks (Fig. 1). Osinski et al. (2005a) suggest that the marcasite here formed at temperatures 100–240 °C and pH <5 during the main stage of the postimpact

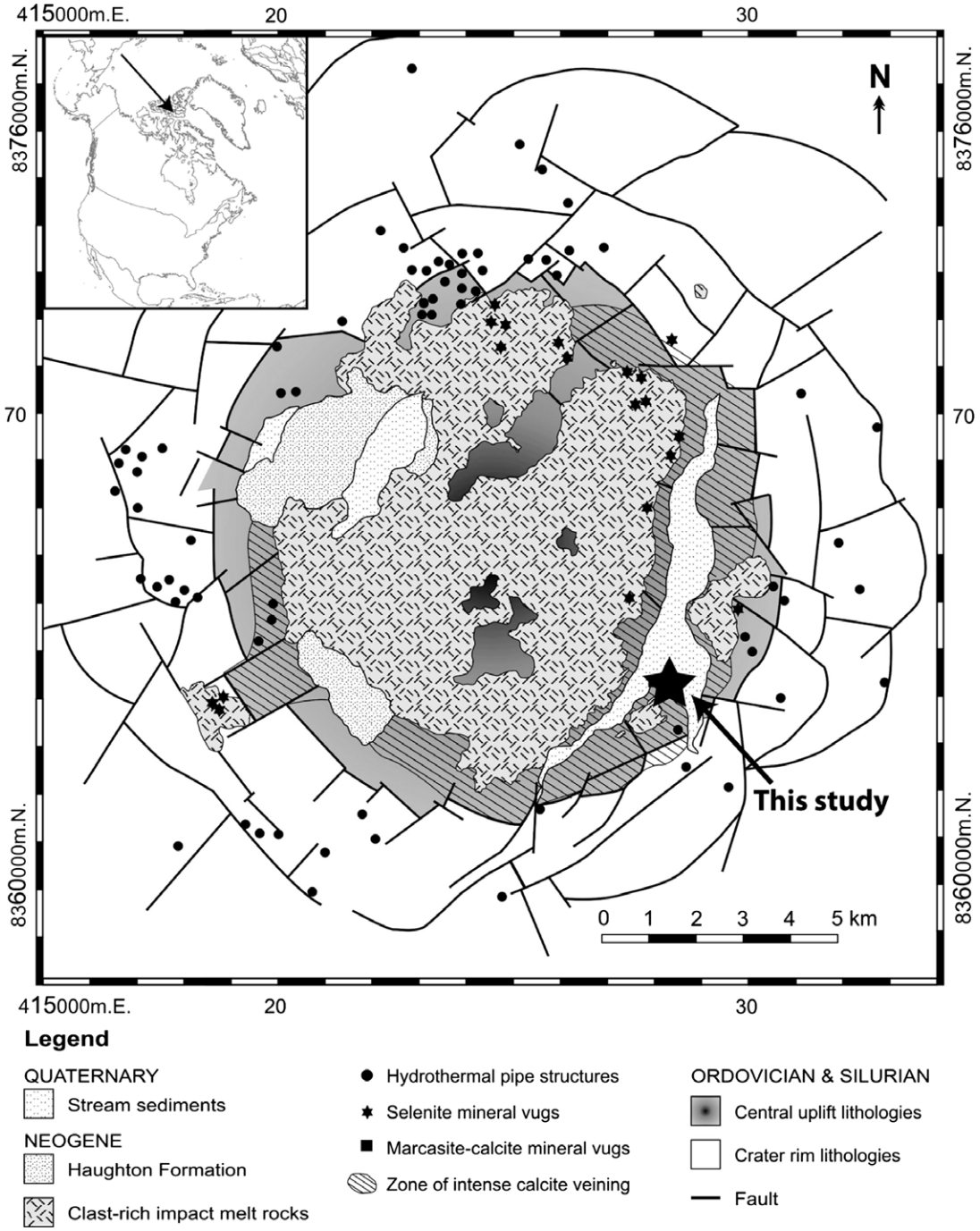

Fig. 1. Geologic map of the Haughton impact structure modified from Osinski et al. (2005a) with the location of the calcite- and marcasite-bearing vug studied here starred. The vug is located within the clast-rich impact melt rocks. The inset in the upper left shows the approximate location of the impact structure.

hydrothermal system. Homogenization temperatures of fluid inclusions within the late-stage calcite from the same vug give similar formation temperatures of 118–210 °C (Osinski et al. 2005a). These minerals formed during the main stages of hydrothermal activity as the system cooled and both liquid and vapor were present (Osinski et al. 2001, 2005a). The sulfides weathered to sulfates and oxides/hydroxides, including copiapite, goethite, jarosite, rozenite, fibroferrite, gypsum, melanterite, and szomolnokite (Izawa et al. 2011). The chemical and redox gradients present at this deposit are thought to be good energy sources for microbes (Izawa

et al. 2011). In addition, isotopic fractionations between sedimentary gypsum and hydrothermal marcasite and pyrite at Haughton are too high to have formed from abiotic processes and rather are likely the result of microbial activity during the hydrothermal system that was active within 10,000 yr of the impact event (Parnell et al. 2010). These microbial signatures are also preserved in the sulfates that formed through weathering of the sulfides (Parnell et al. 2012).

METHODS

Overview

The calcite–marcasite-bearing vug is several meters wide and located within the clast-rich impact melt rocks. This deposit was exposed as the adjacent river systematically eroded into the near-vertical cliff of impact melt rock. The outcrop was imaged in the field with a hyperspectral imager, and five samples representative of the different mineral assemblages visibly identified at the site and located within images of the outcrop were collected. Sample descriptions are given in Table 1. These samples were analyzed with a point spectrometer in the field, and other mineralogical and chemical analyses were completed in the laboratory upon return.

Point Spectroscopy

Point spectra were acquired on various coatings and surfaces of each sample with an Analytical Spectral Devices, Inc. (ASD) Fieldspec 3 from 0.35–2.5 μm with spectral resolutions of 3 nm at 0.7 μm and 10 nm at 1.4 and 2.1 μm. This instrument's sampling intervals are 1.4 nm for wavelengths 0.35–1.0 μm and 2 nm for wavelengths 1.0–2.5 μm, and the software automatically resamples spectra to 1 nm spacing for output. Samples collected from the outcrop were stored on ice within a small cave while in the field to minimize changes in mineralogy or hydration state before ASD spectra were obtained. The measurements were performed in the field using the ASD contact probe attachment, which has its own internal light source and a viewing geometry of approximately 0° incidence and 30° emission angles. Measurements were made relative to Spectralon® and corrected for the reflectance properties of Spectralon® by multiplying by spectrum HL-JFM-012 of SRT-99-050 measured in the Reflectance Experiment Laboratory (RELAB, Brown University, Providence, RI, USA; Pieters 1983) that was resampled to the wavelengths of output ASD spectra.

Table 1. Sample descriptions.

Sample name	Sample description
APDI-13-14a	Yellow, popcorn-textured mixed sulfate
APDI-13-14b	Dark red coating on calcite host rock
APDI-13-14c	Small green marcasite crystals with minor pyrite on calcite host rock
APDI-13-14h	Friable blue-gray phase
APDI-13-14j	Oxidized, dark red, weathered marcasite with the primary textures and morphologies of the marcasite still visible

Hyperspectral Imaging in the Laboratory

All samples collected at the outcrop except APDI-13-14j were imaged at visible-shortwave infrared (VSWIR) wavelengths in the laboratory at Headwall Photonics, Inc. (Fitchburg, MA, USA) using their pushbroom High Efficiency Hyperspec® visible–near-infrared (VNIR) E-series imager (338 spectral channels from 0.4 to 1.0 μm, 7 nm spectral resolution defined as the full width at half maximum of the slit image intensity, 1.785 nm sampling interval) and High Efficiency Hyperspec® shortwave infrared (SWIR) X-series imager (138 spectral channels from 1.0 to 2.5 μm, 12 nm spectral resolution, and 12.0656 nm spectral sampling). Samples were moved through the imaging spectrometers' fields of view on a motorized scanning table that is part of the Hyperspec® Starter Kit™ and illuminated with a quartz tungsten halogen bulb. The lens on the VNIR imager has an instantaneous field of view (IFOV) of 0.382 mrad, corresponding to spatial resolutions up to ~43.5 μm/pixel. The lens on the SWIR imager has an IFOV of 1.2 mrad with achievable spatial resolutions up to ~133 μm/pixel. The imagers viewed the samples from nadir. Where possible, SWIR images were warped to VNIR images using manually selected control points, a first degree polynomial, and nearest neighbor resampling. The VNIR and SWIR images were then joined at 0.997 μm (VNIR) and 0.998 μm (SWIR) and stacked to create a single image cube, deleting overlapping bands and removing any offset between the detectors by multiplying the SWIR image by a factor that assumed no change in reflectance between 0.997 and 0.998 μm. It was not possible to join images of samples with significant surface topography because the changes in distance from the different lenses of the VNIR and SWIR systems led to spatial offsets that could not be removed with simple polynomials. Imaging and calibration methods are described by Greenberger et al. (2015a). Analyses of these images were done through use of spectral (e.g., Clark and Roush 1984; Pelkey et al. 2007; Viviano-Beck et al.

2014) and mineral indicator parameters given in Table S1 in supporting information.

Near-Infrared (NIR) Hyperspectral Imaging in the Field

The outcrop was imaged in the field during the 2013 field season using a Channel Systems near-infrared (NIR) hyperspectral imager. This imaging system is an acousto-optic tunable filter with 10 nm spectral resolution and sampling that measures from 0.65 to 1.1 μm. The dark current signal of the instrument was measured by acquiring an image with the lens cap on, and this image was subtracted from the image of the outcrop before atmospheric correction to remove instrumental effects. Exposure times at each wavelength were determined using the imager's autoexpose function that maximizes the exposure time at each wavelength without saturating. The exposure times were saved, and the images where light reached the sensor (i.e., all but the dark current images) were normalized to account for the varying exposure times as the signal received scales linearly with exposure time for images where light reaches the sensor. Dark current measurements are independent of exposure time, and the dark images therefore were not normalized for exposure times (i.e., the raw signal from the dark measurements was subtracted from the raw signal of the outcrop and white images; see equation below). Images were calibrated through a dark object subtraction using the minimum measurement of any pixel within the image at each wavelength, which was assumed to be the additive contribution to the signal from atmospheric scattering (Vincent 1972; Chavez 1988, 1996, and references therein). Then, the image was calibrated to reflectance by dividing by the spatially averaged signal received from a Spectralon® panel within an image taken next to the outcrop and multiplied by the same spectrum of Spectralon® used in the ASD calibration but resampled to the wavelengths sampled by this imager. The calibration to reflectance (R) was done using the following equation:

$$R = \frac{\frac{S_{ds} - Do}{t_o}}{\frac{W_{ds} - D_{ds}}{t_s}} * R_s,$$

where S_{ds} is the signal in the image of the outcrop after subtracting the signal from the dark image at each pixel, D_o is the dark object spectrum described above for the outcrop image, t_o are the exposure times at each wavelength for the image of the outcrop, W_{ds} is the average signal from the image of the Spectralon® panel after subtracting the dark current at each pixel, D_{ds} is the dark object spectrum from the image of the Spectralon® panel, t_s are the exposure times at each wavelength for the image of the Spectralon® panel, and R_s is the reflectance spectrum of Spectralon® measured in RELAB. These methods are similar to calibration of AVIRIS data using the methods of Clark et al. (2002). In total, five images of the outcrop were acquired.

Lithologies were mapped within the hyperspectral images using spectral parameters (e.g., Clark and Roush 1984; Pelkey et al. 2007; Viviano-Beck et al. 2014) and lithological indicators, which are combinations of spectral parameters (Table S2 in supporting information). These parameters and indicators were derived using spectra from the NIR image of the samples that were later collected from within the scene and analyzed in the laboratory, and the parameters were further refined to ensure that obviously different lithologies (i.e., different color or morphology in photographs, different appearance in NIR false color composites, or different spectral characteristics) were not mapped by the same parameters. The equations were developed using spectra of rock surfaces, not powders. In the wavelength range sampled by the NIR imager, spectra at this outcrop show electronic transitions and intervalence charge transfers of transition metal cations, Fe^{2+} and Fe^{3+} (e.g., Burns 1993). Here, Fe sulfides, sulfates, and oxides are known to be present (Izawa et al. 2011), and variations in the shape, center wavelength, width, and slope of these features at the wavelengths sampled by the imager are due to the differences in Fe mineralogy. Different mapped units correspond with the samples that were collected and, using the ASD spectra and spectra from the images of the known sampling locations, spectrally similar materials were mapped across the outcrop. Spectral parameters given in Table S2 calculate depths of absorption features and slopes. Parameters mapping lithologies consistent with the samples collected, also given in Table S2, were determined through an iterative process where combinations of spectral parameters are used to relatively uniquely map spectrally similar materials.

Major Element Chemistry Analyses

Major element chemistries for samples collected at the outcrop were determined through inductively coupled plasma–atomic emission spectroscopy (ICP-AES) analyses at the Brown University Environmental Chemistry Facilities following a flux fusion sample preparation for Al, Ca, Cr, Fe, K, Mg, Mn, Na, Ni, P, Si, and Ti content using methods modified from Murray et al. (2000), with complete details given by Greenberger et al. (2015a). Standard reference materials (NIST2711, MAG-1, DTS-2B, NIST1646a, BIR-1, SGR-1, BHVO-

2, NIST2702, BCR-2, G-2, and NIST1c) and blanks were run with the same methods as unknown samples. Solutions of fused beads quenched in 10% nitric acid were analyzed on a JY2000 Ultrace ICP-AES using intensities for peaks given in Murray et al. (2000), and a solution with intermediate composition was run initially and periodically throughout the analysis to correct for instrumental drift with time. Concentration data were determined after correcting for instrument drift and subtracting blanks using linear regression curves from the standard reference materials. One sample was run in duplicate, and two were run in triplicate. Average errors as determined by standards that were run as unknowns were typically <5% as a percentage of the actual concentrations or <0.03 wt% in actual concentration. Standard deviations reported here are in some cases higher likely due to sample heterogeneity for small volume samples (i.e., coatings). Analysis results are reported in oxide weight percentages to be consistent with geochemical convention. However, some Fe is in sulfides and is coordinated by S, not O.

The carbon content of the samples was measured with elemental analyses on a CE Instruments Model NC2100 Elemental Analyzer. Samples were prepared by weighing 8–10 mg of each into tin capsules, which were then folded and crushed. Two blanks were run, and varying amounts of four standards (acetanilide, cyclohexane, pine–SRM 1575, and Montana soil–SRM 2711 for all samples but APDI-13-14j and sulfanilamide for APDI-13-14j) were analyzed to calculate regression curves and to check the quality and consistency of the measurements. Typical errors on these measurements are <10%.

X-bay Diffraction (XRD)

Bulk powdered samples were prepared for powder X-ray diffraction (pXRD) analyses using a back-packing method and measured on a Rigaku rotating-anode XRD with Co Kα radiation operated at 45 kV and 160 mA. With this instrument, monochromation is achieved with a curved crystal, diffracted beam, and graphite monochromator, and X-rays were collimated with 1° divergent and scatter slits and a 0.15 mm receiving slit. Samples were scanned from 2 to 82° 2θ with 0.020 steps at a rate of 10° 2θ/min. Mineralogies of coatings were determined using micro-X-ray diffraction (μXRD; Flemming 2007) with no sample preparation on a Bruker D8 Discover μXRD. A 60 mm Co Gobel Mirror with a 300 μm snout provides a nominal 300 μm beam diameter. This instrument has an area detector, and each sample was scanned in omega (ω) scan mode with two frames. The parameters for the first frame were $\theta_1 = 15°$, $\theta_2 = 20.5°$, and $\omega = 10$, and this scan ran for 90 minutes. The second frame was acquired over 145 minutes with the following parameters: $\theta_1 = 34.5°$, $\theta_2 = 40°$, and $\omega = 19$. ω is the degree of rotation of both source and detector in a clockwise direction during analysis. The two frames were converted to two-dimensional XRD patterns and combined to obtain continuous measurements from 14° to 95° 2θ in Diffrac.Suite EVA software (https://www.bruker.com/products/x-ray-diffraction-and-elemental-analysis/x-ray-diffraction/xrd-software/overview/eva.html). Mineralogies from pXRD and μXRD patterns were determined by comparing peak positions of the unknowns with diffraction patterns from the International Centre For Diffraction Data (ICDD) database through an interface in the software package EVA.

RESULTS

Individual Sample Analyses

ASD spectra of sample APDI-13-14a (Table 1; Fig. 2) have electronic transitions of Fe^{3+} at 0.42, 0.55, and 0.82 μm consistent with the Fe^{3+}-bearing sulfate minerals fibroferrite and copiapite/ferricopiapite (Crowley et al. 2003; Cloutis et al. 2006). Copiapite and ferricopiapite have spectra that are nearly identical in this wavelength range and cannot be distinguished with VSWIR spectroscopy alone (Cloutis et al. 2006); however, the pXRD results are more consistent with copiapite. A deep 0.55 μm electronic transition suggests that fibroferrite is also present (Crowley et al. 2003). The shape and positions of deep absorption features from OH and H_2O are generally consistent with these mineral identifications and include (1) a broad, complex feature around ~1.4–1.6 μm composed of overlapping absorptions at ~1.44, 1.49, and 1.55 μm (due to the OH stretching overtone of OH and H_2O [Crowley et al. 2003; Cloutis et al. 2006]); (2) a broad, weak feature around 1.77 μm consistent with a H_2O-bearing sulfate (Cloutis et al. 2006); and (3) a strong feature due to a H-O-H combination band at 1.93 and 1.99 μm (Hunt et al. 1971; Clark et al. 1990; Cloutis et al. 2006). Flattening of the spectra from 2.1 to 2.3 μm may be due to weak combination bands related to metal-OH bonds and SO_4 (e.g., Cloutis et al. 2006), but individual features are too poorly defined to determine the exact band centers and assignments. Overall, these overtones and combination tones of vibrational absorption features in our reflectance spectra are consistent with copiapite and fibroferrite (e.g., Crowley et al. 2003; Cloutis et al. 2006). Bearing in mind that the ASD measures a larger area, sometimes averaging multiple components within a single spectrum, hyperspectral imaging allows us to obtain spectra of much smaller

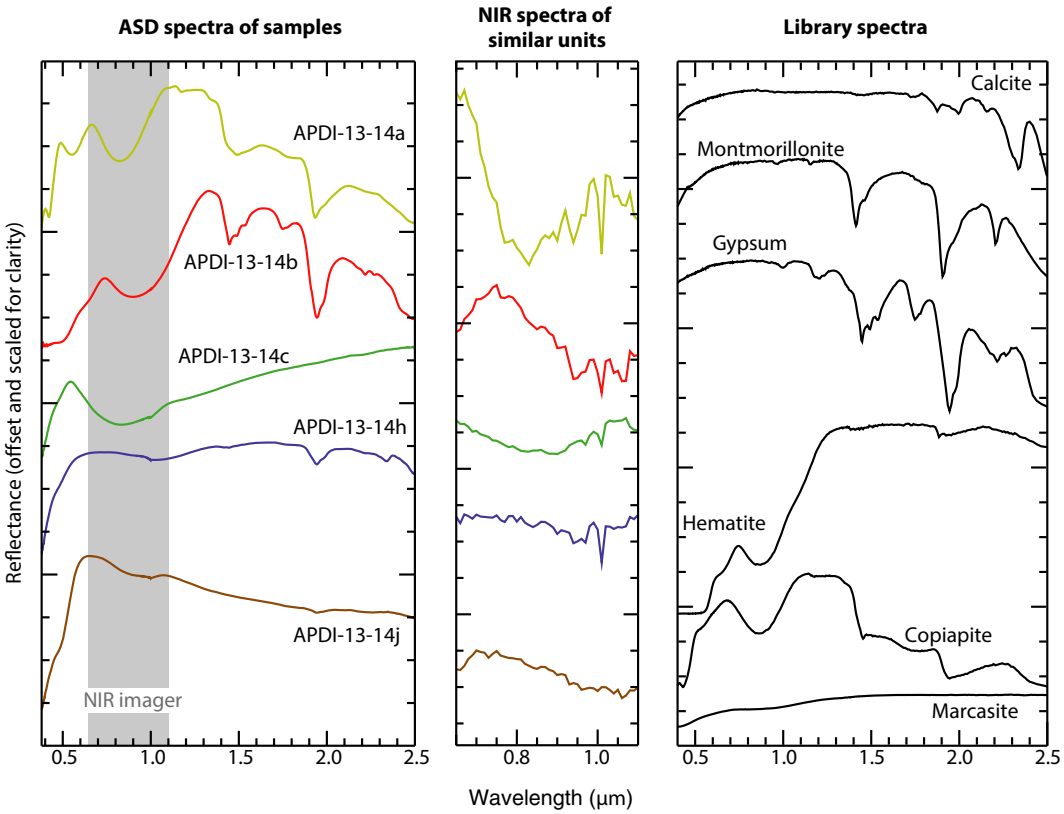

Fig. 2. left) Reflectance spectra of samples measured in the field with an ASD with contact probe attachment. middle) Reflectance spectra from the NIR images of similar units to those sampled and measured with the ASD. The colors match the corresponding ASD spectra and the units mapped in Fig. 5. (right) Library spectra of some minerals present in the samples analyzed here. Copiapite (GDS21), hematite (GDS27), gypsum (SU2202), montmorillonite (STx-1), and calcite (CO2004) spectra are from the USGS spectral library (Clark et al. 2007). The marcasite spectrum (MAR101) is from the RELAB database (Pieters 1983) and was originally reported by Cloutis and Gaffey (1994). Spectra in all plots are offset and scaled for clarity.

areas (100s of micrometers) within single pixels and thereby identify additional phases. A VSWIR hyperspectral image of this sample (Fig. 3a) shows small areas of spectrally distinct gypsum, which is readily identified by its characteristic triplet absorption feature at 1.4 μm (e.g., Hunt et al. 1971; Clark et al. 1990). Mineral identifications of copiapite, fibroferrite, and gypsum are confirmed by pXRD. pXRD also identifies melanterite, which was not identified with spectroscopy, perhaps due its low abundance. Another possibility is that the melanterite may be finely disseminated within the sample, and its spectral signature could be masked by the other phases that are present and have strong spectral features. Cull-Hearth et al. (2016) identified shifts in the positions of copiapite absorption features when mixed with melanterite, particularly a longward shift of the 0.866 μm feature. The spectra measured here do not show evidence for those shifts likely due to the presence of fibroferrite as well, which should cause a shift in the opposite direction for the 0.866 μm feature. The sample cation chemistry is dominated by Fe with minor Ca, consistent with the identification of Fe-bearing sulfates (copiapite/ferricopiapite and fibroferrite) with minor gypsum.

ASD spectra of sample APDI-13-14b (Table 1; Fig. 2) exhibit absorptions from electronic transitions of Fe^{3+} centered around 0.93–0.95 μm and 0.51 μm that may arise from a Fe^{3+}-oxide or -sulfate, such as goethite or jarosite (e.g., Burns 1993; Scheinost et al. 1998; Cloutis et al. 2006), though spectra lack other SWIR features due to jarosite. Based on μXRD results, these spectral characteristics are consistent with a combination of both goethite and jarosite. In the SWIR, these spectra have a well-expressed triplet at 1.4–1.7 μm from OH stretching overtones that match gypsum (e.g., Hunt et al. 1971; Clark et al. 1990). Additional absorption features at 1.75/1.77 μm, 1.94/1.98 μm (H_2O combination band), 2.17–2.18 (S-O overtone or OH/H_2O combination or overtone), 2.22 (S-O overtone or OH/H_2O combination or overtone), 2.27 (S-O overtone or OH/H_2O combination or overtone), 2.43 (S-O overtone), and 2.48 μm (S-O

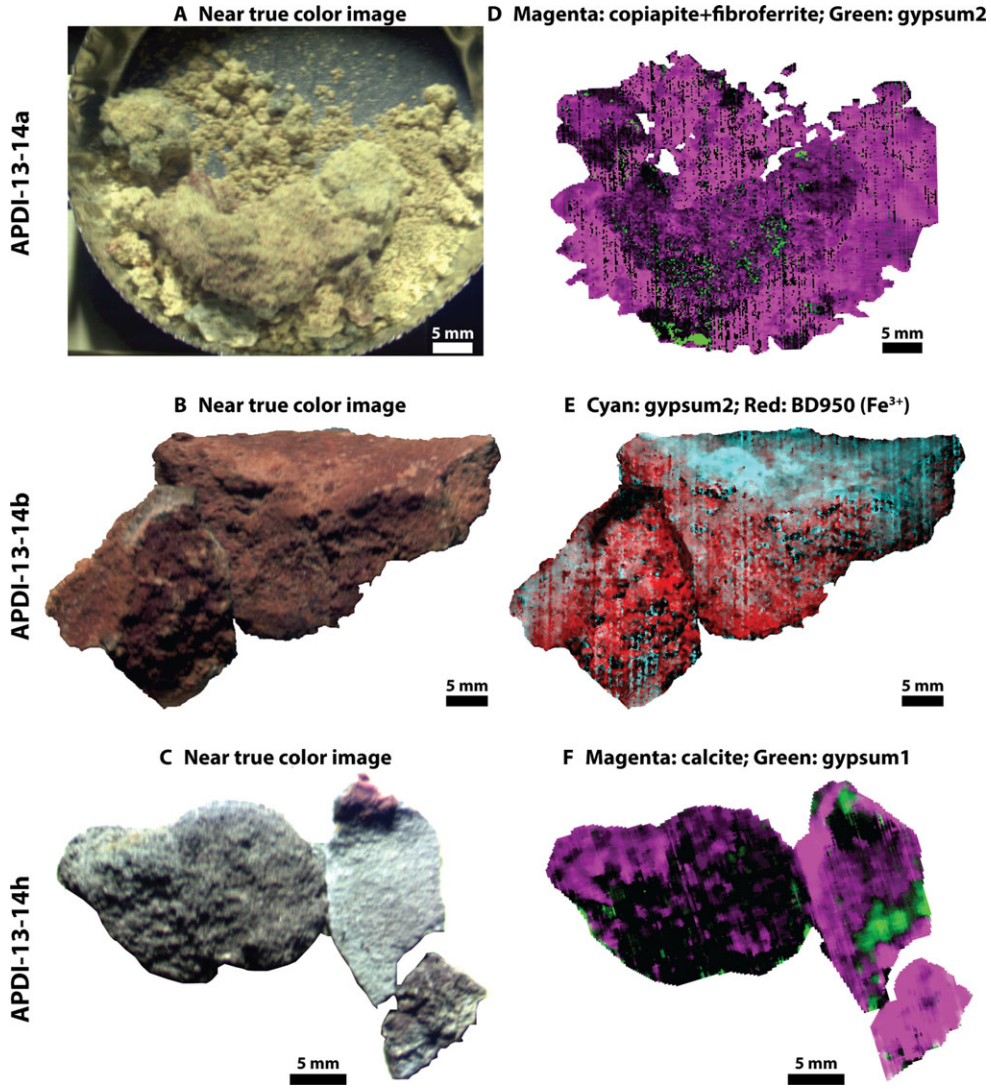

Fig. 3. Hyperspectral images of three samples measured in the laboratory. A–C) Color composite images with bands selected to approximate a true color image for samples (A) APDI-13-14a, (B) APDI-13-14b, and (C) APDI-13-14h. Red: 0.666 μm, green: 0.534 μm, blue: 0.427 μm. D) Mineral indicator map of sample APDI-13-14a. Magenta: fibroferrite + copiapite, green: gypsum2. E) Spectral parameter and mineral indicator map of sample APDI-13-14b. Cyan: gypsum2. Red: BD950 (due to Fe^{3+}). F) Mineral indicator map of sample APDI-13-14h. Magenta: calcite. Green: gypsum1. See Table S1 for descriptions of each parameter. The parameters shown in (E) and (F) have been median filtered to reduce noise.

overtone), all confirm the identification of gypsum (e.g., Hunt et al. 1971; Clark et al. 1990; Cloutis et al. 2006). Hyperspectral imaging also shows that this coating is composed of fine-grained Fe^{3+}-oxides, Fe^{3+}-sulfates, and gypsum, with variations in the relative strengths of absorption features likely due to variations in the relative abundances of these phases (Fig. 3b). The chemical composition of this sample is more complex than APDI-13-14a, with a large component of Ca in addition to Fe (Table 2). Carbon is detected in this sample and is likely due to contributions from the calcite on which this coating precipitated. μXRD identifies gypsum, jarosite, akaganeite, and goethite in these coatings (Table 2). pXRD also identifies pyrite, quartz, calcite, and marcasite. Some interior faces not in the field of view of the NIR hyperspectral data have visually identified marcasite and likely also pyrite, are not the coatings mapped in the NIR hyperspectral data, and were not targeted for measurement by μXRD.

The reflectance spectrum of APDI-13-14c (Table 1; Fig. 2) exhibits a crystal field absorption feature centered around 0.83–0.84 μm due to Fe^{2+} and is roughly consistent with marcasite (Hunt et al. 1971; Cloutis and Gaffey 1994). ASD spectra of other portions of the sample indicate the presence of calcite

Table 2. Chemical compositions (ICP-AES and elemental analyses) in wt% with standard deviations given for measurements with multiple replicates, tentative identifications with VSWIR spectroscopy, and mineralogy from pXRD and/or μXRD for samples discussed in the text. Reported compositions are averages for samples with replicate analyses.

	APDI-13-14a	APDI-13-14b	APDI-13-14c	APDI-13-14h	APDI-13-14j
Replicates	2	1	3	3	1
Al_2O_3	0.15 ± 0.02	0.31	0.14 ± 0.01	2.97 ± 0.12	0.07
CaO	2.40 ± 0.01	18.78	18.60 ± 0.61	38.60 ± 0.94	3.93
Cr_2O_3	0.001 ± 0.000	0.001	n.d.	0.002 ± 0.000	0.001
FeO	25.86 ± 0.06	28.08	25.97 ± 3.85	2.54 ± 0.26	38.79
K_2O	0.08 ± 0.01	0.14	0.06 ± 0.01	1.78 ± 0.09	0.03
MgO	0.84 ± 0.00	0.47	0.72 ± 0.06	2.13 ± 0.08	0.13
MnO	0.001 ± 0.00	0.005	0.005 ± 0.000	0.012 ± 0.000	0.002
Na_2O	0.018 ± 0.027	n.d.	0.002 ± 0.011	0.022 ± 0.008	n.d.
NiO	0.001 ± 0.000	n.d.	n.d.	0.001 ± 0.000	0.002
P_2O_5	0.01 ± 0.02	0.01	0.01 ± 0.01	0.05 ± 0.01	0.01
SiO_2	0.99 ± 0.00	2.01	1.15 ± 0.03	18.52 ± 1.14	0.69
TiO_2	0.005 ± 0.000	0.009	0.004 ± 0.001	0.128 ± 0.010	n.d.
C	0.06 ± 0.02	2.99	3.05 ± 0.12	8.11 ± 0.10	1.77
Mineralogy	*VSWIR:* Fft, Cop, minor Gp *pXRD:* Fft, Cop, Gp, Mlt	*VSWIR:* Gp, Fe^{3+}-oxide or sulfate *μXRD (coating):* Gp, Jrs, Gth, Akg *pXRD:* Cal, Gp, Mrc, Py, Qz	*VSWIR:* Mrc *μXRD:* Mrc *pXRD:* Mrc, Cal, Py, Clt, Gp, Qz	*VSWIR:* Fe^{2+}-clay/sulfate, Al-clay, Gp, Cal *pXRD:* Qz, Cal, Mc, Gp, Hem, Ilt, Mnt	*VSWIR:* Mrc, Jrs or Gth *μXRD:* Gp, Jrs, Mrc

n.d. = not detected, Mineral abbreviations (from Whitney and Evans [2010] where possible), endmember chemical formulas, and best matching ICDD card numbers: Akg = akaganeite ($Fe^{3+}O(OH,Cl)$; 00-042-1315), Cal = calcite ($CaCO_3$; 01-083-1762), Clt = celestine ($SrSO_4$; 00-005-0593), Cop = copiapite ($Fe^{2+}Fe^{3+}{}_4(SO_4)_6(OH)_2{\cdot}20H_2O$; 00-035-0583), Fft = fibroferrite ($Fe^{3+}(SO_4)(OH){\cdot}5H_2O$; 01-083-1803), Gp = gypsum ($CaSO_4{\cdot}2H_2O$; 00-036-0432), Gth = goethite ($Fe^{3+}OOH$; 00-029-0713); Hem = hematite (Fe_2O_3; 00-003-0800); Ilt = illite ($KAl_2(Si_3Al)O_{10}(OH)_2$; 00-010-0490), Jrs = jarosite ($KFe^{3+}{}_3(SO_4)_2(OH)_6$; 00-002-0602), Mc = microcline ($KAlSi_3O_8$; 00-022-0675), Mlt = melanterite ($Fe^{2+}SO_4{\cdot}7H_2O$; 00-022-0633), Mnt = montmorillonite ($(Na,Ca)_{0.3}(Al,Mg)_2Si_4O_{10}(OH)_2{\cdot}nH_2O$; 00-007-0051), Mrc = marcasite (FeS_2; 00-037 = 0475), Py = pyrite (FeS_2; 01-073-8127), Qz = quartz (SiO_2; 00-005-0490).

on which the marcasite precipitated and gypsum. The high Fe concentration measured through chemical analyses is consistent with the spectral interpretation of marcasite (Table 2). There is also significant Ca in this sample, which is likely from the calcite-rich host rock that was not completely removed during sample preparation. μXRD data of two points on the surface of the sample identify only marcasite. The powdered sample for pXRD indicated other phases in the larger rock, including calcite, celestine, pyrite, gypsum, and quartz.

APDI-13-14h spectra (Table 1; Fig. 2) have weak, broad absorption features arising from electronic transitions of Fe^{2+} centered at ~0.9 and 1.1 μm, which is potentially in an Fe^{2+}-bearing phyllosilicate or a sulfate such as glauconite or rozenite (Crowley et al. 2003; Cloutis et al. 2006). Spectra also indicate some gypsum identified by a weak triplet from OH stretching overtones near 1.4–1.5 μm and the shape of the 1.9 μm absorption band (e.g., Hunt et al. 1971; Clark et al. 1990). The absorption feature at 2.21 μm may be the result of an Al-OH combination in a clay such as montmorillonite or illite, from an OH/H_2O combination or S-O overtone in gypsum, or both (e.g., Clark et al. 1990; Cloutis et al. 2006) or could also result from minor water in quartz (Aines and Rossman 1984; Goryniuk et al. 2004). Finally, the deeper 2.34 μm absorption feature is a C-O combination in calcite (Hunt and Salisbury 1971). Interpretations of spectroscopy suggest that this sample is a mixture of Fe^{2+}- and Al-bearing clays, calcite, and gypsum with possible hydrated silica. While most of the sample is dominated spectrally by calcite, VSWIR imaging spectroscopy identifies small areas with more gypsum (Fig. 3c). Chemical analyses show high Ca and relatively high Si compared with other samples from this site along with some Mg and K (Table 2). The Fe content of this sample is quite low relative to others from this site. pXRD analyses identify quartz, microcline, and hematite in addition to phases identified through spectroscopy (Table 2). There are likely both smectite and illite clays present, and a clay such as glauconite is consistent with the pXRD pattern and could explain the Fe^{2+} feature in the spectra.

Spectroscopy of APDI-13-14j (Table 1) shows a peak in reflectance (0.65 μm) at longer wavelengths than the marcasite sample APDI-13-14c (0.54 μm) attributed to partial oxidation (Fig. 2). There is also a weak Fe^{3+} electronic transition absorption feature at 0.48 μm in APDI-13-14j and a stronger crystal field absorption feature centered at 0.87–0.90 μm that may result from the convolution of the underlying marcasite with a Fe^{3+}-oxide such as goethite, which has a Fe^{3+} electronic transition at 0.95 μm (Scheinost et al. 1998), or a Fe^{3+}-sulfate such as jarosite. The spectrum has a negative slope into the infrared that is often observed with fine-grained coatings, where the bright coating dominates the spectrum at the shortest wavelengths but is more transparent at longer wavelengths (Singer and Roush 1983; Fischer and Pieters 1993; Johnson and Grundy 2001). The negative slope may also result from Rayleigh scattering of extremely fine particles (Clark et al. 2008; Brown 2014). H-O-H combination bands are seen at 1.9 μm along with a very weak, broad feature at ~2.20–2.27 μm from S-O or OH/H_2O overtones or combination bands that are too weak and poorly defined to assign to a specific mineralogy (e.g., Clark et al. 1990; Cloutis et al. 2006). This sample is chemically similar to APDI-13-14c, though with higher Fe and lower Ca, likely due to a lower proportion of the calcite host rock powdered with the sample (Table 2). μXRD analyses of the sample surface identify gypsum and jarosite in addition to marcasite, though low abundances of Ca and K suggest that the gypsum and jarosite are minor phases.

Outcrop Imaging and Mapping

The outcrop units spectrally similar to the samples described above were mapped with the NIR imaging spectroscopy. The spectra from the NIR imager (Fig. 2) are relatively consistent with ASD spectra of corresponding units, with slight differences in overall slopes probably due to artifacts from the atmospheric correction, differences in viewing geometry between the Spectralon® panel used for calibration and the outcrop, or differences in the precise spatial area sampled. However, these differences occur in all spectra, and there is remarkable consistency between spectra of the same materials present across the images. In these data, variations in the positions of Fe^{2+} and Fe^{3+} electronic transitions and slopes result from differences in mineralogy between the units.

Spectral parameters (Table S2) were used to map spectrally similar units, an example of which is shown in Fig. 4. These units were drawn onto a photograph of the outcrop (Fig. 5). Several key relationships between phases are identified. Large areas of marcasite (green) and oxidized marcasite (brown) occur on the roof of the vug. The oxidized marcasite sometimes occurs entirely within the unaltered marcasite and sometimes occurs along the edges of the marcasite. The mixed sulfate phase (yellow) is often found on flat areas below the marcasite, and the red coating (red) generally is present immediately below the mixed sulfates. Only one small patch of the blue-gray phase (blue) is identified.

DISCUSSION

The focus of our investigations is a vug in which there has been significant hydrothermal mineralization within the clast-rich impact melt rocks of the Haughton impact structure. Using imaging spectroscopy of this outcrop, we map the spatial distributions of primary and secondary assemblages to understand the formation pathways and the habitability of the site. The primary hydrothermal mineralogies identified here are calcite and marcasite. Secondary weathering products include a mixture of fibroferrite and copiapite; a gypsum, akaganeite, goethite, and jarosite coating on the calcite host rock; oxidized marcasite with formation of a thin Fe^{3+}-oxide and sulfate coating; and a blue-gray phase that is a mixture of calcite, gypsum, clay minerals, microcline, quartz, and hematite. The mineralogical and chemical analyses show remarkable agreement: the cation composition of samples APDI-13-14a, APDI-13-14c, and APDI-13-14j are dominated by Fe, consistent with mineral identifications; sample APDI-13-14b contains Fe- and Ca-bearing minerals and chemically contains significant Fe and Ca; and both the mineralogy and chemistry of APDI-13-14h are more complex. The mineral identifications are similar to those reported for the same site by Izawa et al. (2011) with the exception of jarosite, which was only identified as a minor component in the coatings of APDI-13-14b and APDI-13-14j, likely because the locations within the outcrop where jarosite has previously been found as a major component were not sampled and/or they had mostly been removed by previous sampling. Our work extends the work of Izawa et al. (2011) by measuring the spectroscopic properties of these samples and using imaging spectroscopy in the field to map the distributions of these mineral assemblages in order to gain insight into the alteration processes.

Inferred Water–Rock Interactions

The results of mapping of secondary phases using NIR imaging spectroscopy (Fig. 5) show spatial relationships between different sulfur-bearing assemblages that illuminate changing conditions during the postimpact hydrothermal alteration and subsequent

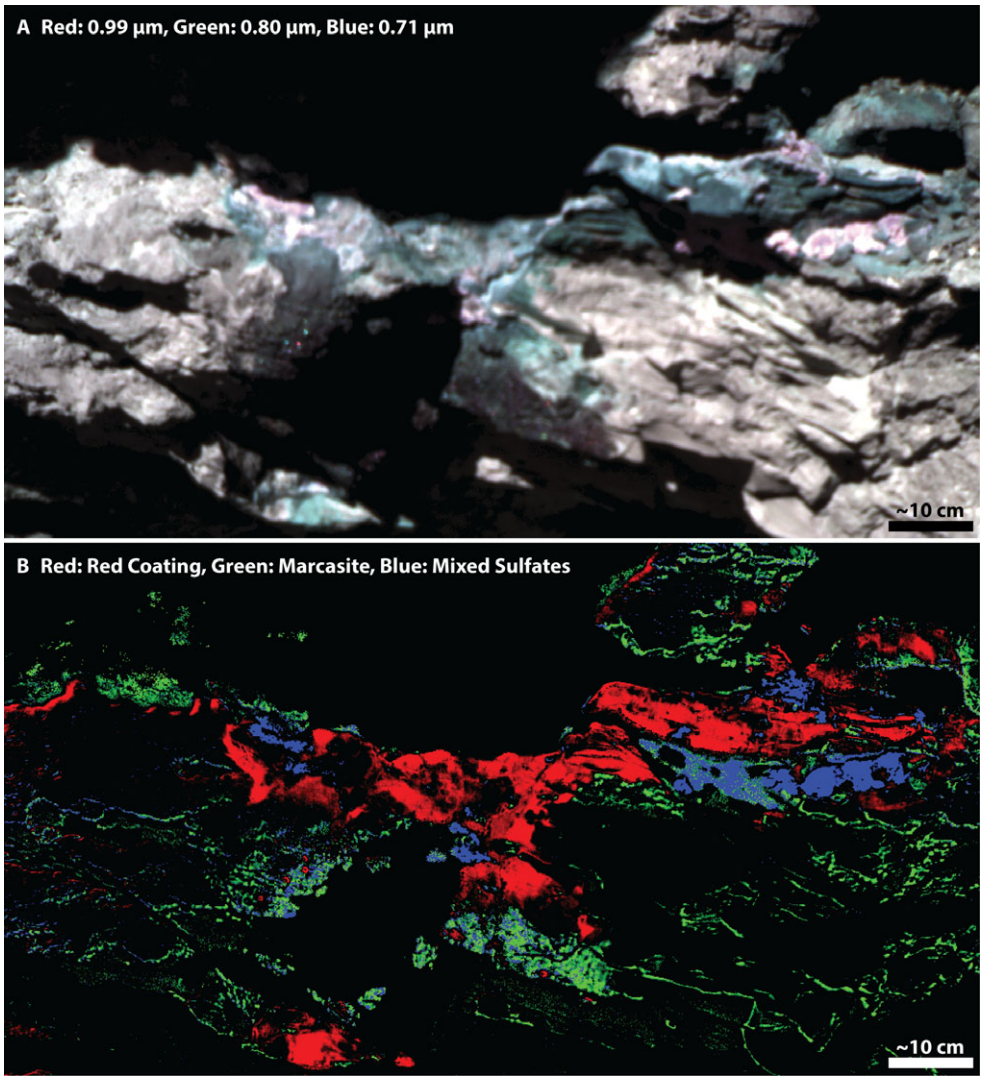

Fig. 4. A) Example NIR false color composite image of one portion of the outcrop. Red: 0.99 μm, green: 0.80 μm, blue: 0.71 μm. B) Example lithological indicator parameter image of the outcrop. Red: red coating, green: marcasite, blue: mixed sulfate. Dark/shadowed areas have been masked in both images. See Table S2 for descriptions of each parameter. The location of this image within the outcrop is shown in Fig. 5A.

low temperature weathering (summarized in Fig. 6). Marcasite formed from the impact-generated hydrothermal system (Osinski et al. 2001, 2005a). The sulfur within the marcasite was likely sourced from the gypsum- and anhydrite-rich Bay Fiord Formation in the target rocks during postimpact fluid circulation (Osinski et al. 2001). This formation, which is part of the impact structure's central uplift, outcrops nearby and underlies the impact melt-rich breccia at this location based on field and orbital mapping (Osinski et al. 2005b; Tornabene et al. 2005). The marcasite at this site was interpreted by Osinski et al. (2001, 2005a) to have formed at temperatures of ~100–240 °C and pH <5. The presence of both Fe^{2+} and sulfide cations in the initial fluids from which the marcasite precipitated require reducing conditions. The marcasite that has been preserved and unweathered is mostly located on overhanging and sloped surfaces such as the roof of the outcrop where contact with altering fluids is relatively limited. Nevertheless, regions with enhanced fluid flow show distinct mineralogic and spectroscopic signatures (mapped in brown as the oxidized marcasite unit containing gypsum and jarosite in Fig. 5). We interpret this assemblage as forming in situ at low temperatures and under more oxidizing conditions, allowing for partial oxidation of Fe and S. An assemblage of gypsum and jarosite is predicted to form at pH ~2–4 (Elwood Madden et al. 2004), and these coatings likely formed from fluids in that pH range with acidity derived from oxidation of the primary marcasite. The

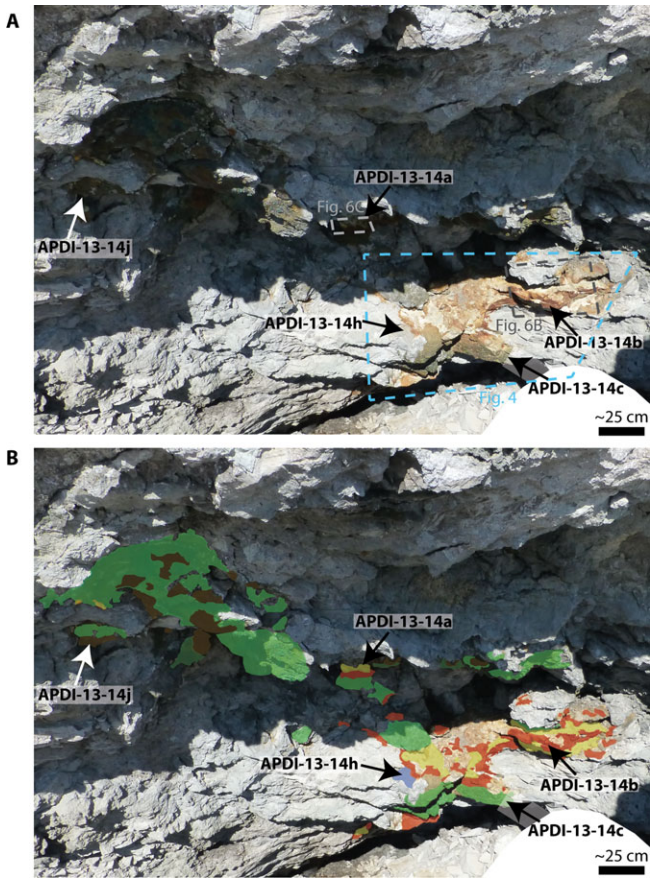

Fig. 5. Map of different mineral assemblages within this vug. A) Photograph of the vug with locations from which samples were collected labeled. Boxes outline the regions shown in Fig. 4 (light blue), 6B (dark gray), and 6C (light gray). B) Mineral assemblages that are spectrally similar to the collected samples. Yellow regions are mixed sulfates similar to APDI-13-14a, red regions are red coatings similar to APDI-13-14b, green regions are unaltered marcasite similar to APDI-13-14c, brown regions are oxidized marcasite similar to APDI-13-14j, and blue is the blue-gray phase spectrally similar to APDI-13-14h.

very thin nature of the coating and limited extent of alteration suggest that volumes of water involved in the alteration were likely very low, and we note that these small amounts of fluids may have quickly reached equilibrium with the surrounding marcasite, impeding further alteration. The location of this oxidized material nearly exclusively on overhanging portions of the outcrop is consistent with the interpreted low water/rock ratios because there is nowhere for water to pool and remain in contact with the marcasite for extended periods of time. Weathering of the marcasite may be further hampered by kinetic effects if reaction rates are slow.

The efflorescent popcorn-textured mixed sulfate phase (yellow in Fig. 5) often occurs on flatter surfaces below the overhanging rocks coated with marcasite. This physical location suggests fluids dripped onto these surfaces after interacting with the marcasite resulting in precipitation of these mixed sulfates. The chemical composition of this phase is dominated by Fe, SO_4, and OH/H_2O. The sulfur in these samples is entirely oxidized, and Fe occurs in both +2 (copiapite and melanterite) and +3 (copiapite and fibroferrite) valence states. The chemical components of this sample likely derive mostly from the marcasite with little interaction with the surrounding calcite-rich rock, which would have resulted in incorporation of significant Ca into the sample mineralogy. There is only 2.4 wt% CaO identified, and laboratory imaging spectroscopy maps a minor component of gypsum. However, the dominant mineralogies in this sample are fibroferrite and copiapite, neither of which contains Ca. The oxidation of the primary marcasite produces sulfuric acid (e.g., Jambor et al. 2000), and pH values of approximately −1 are reported in the literature for waters associated with copiapite (Jambor et al. 2000; Jamieson et al. 2005). These low pH values may result from evaporative concentration of H^+ and other cations (Nordstrom et al. 2000), particularly given the overall low volumes of fluids at the site. In summary, this mixed sulfate phase likely formed at ambient temperatures from extremely low pH fluids that resulted from oxidation of marcasite (Fig. 6). These fluids are more oxidizing than the fluids that formed the marcasite, containing Fe^{2+}, Fe^{3+}, and SO_4^{2-} in solution.

Next, we propose that some of the copiapite and fibroferrite dissolved. The reaction between these acidic fluids and the calcite host rock dissolved some calcite, leading to addition of Ca^{2+} cations to the fluids and neutralizing the acid somewhat. These water–rock interactions resulted in precipitation of gypsum and Fe^{3+}-oxide and sulfate-bearing coatings on the calcite rock directly below the mixed sulfate phases from less acidic fluids with Fe^{3+}, SO_4^{2-}, and Ca^{2+} in solution as well as extremely minor K^+. A phase diagram presented by Elwood Madden et al. (2004) for the Fe-S-Ca-Na-HCO_3-H_2O system predicts an assemblage of gypsum and jarosite at pH ~2–4, and akaganeite dominates at pH 3–7 (Bibi et al. 2011). Thus, a pH of ~3–4 is likely for the fluids forming this red coating. While still acidic, the inferred pH is well above the -1 value expected for copiapite (Jambor et al. 2000; Jamieson et al. 2005). The neutralization of acidic fluids by calcite and formation of gypsum coatings are also observed in acid mine drainage systems (e.g., Booth et al. 1997; Jamieson et al. 2005; Chou et al. 2013; Lindsay et al. 2015).

The blue-gray material is more difficult to fit into the context of these other units, in part because it is confined to one discrete patch at the outcrop. It may

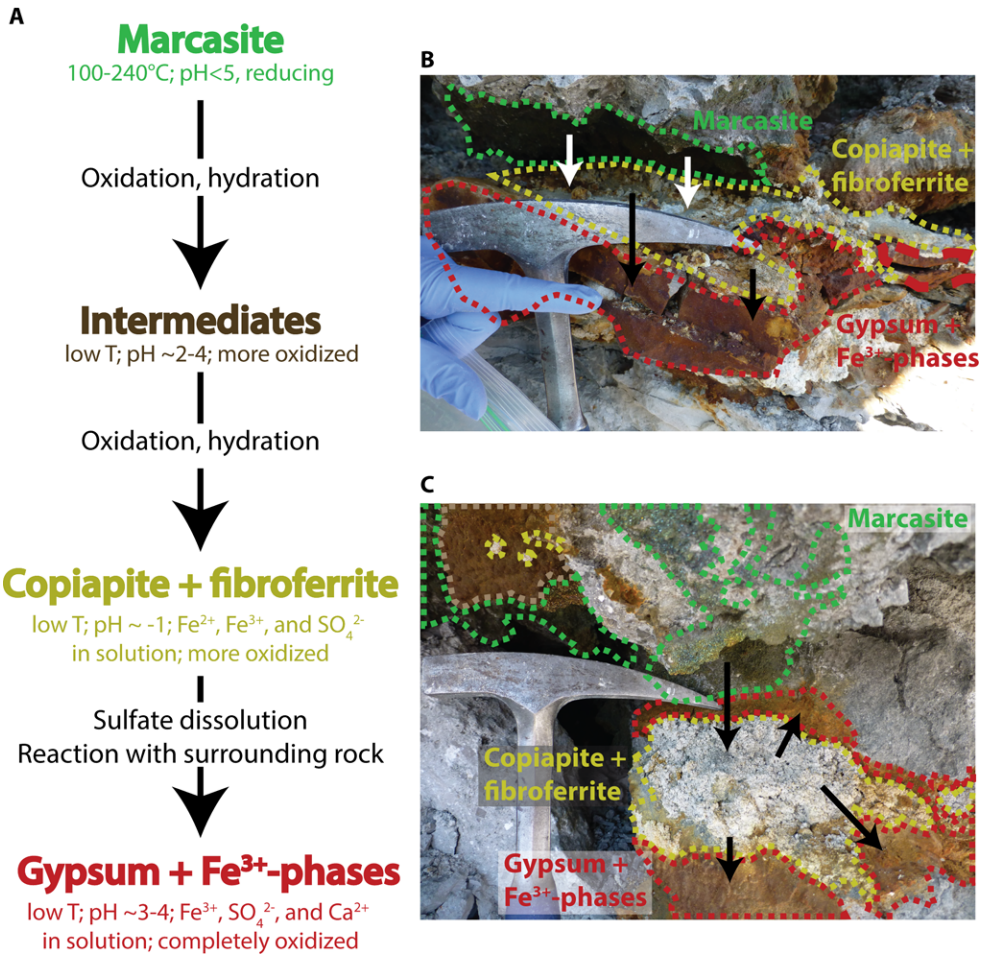

Fig. 6. A) Alteration sequence inferred from the results of this paper. Of the minerals represented, only marcasite formed in the postimpact hydrothermal system, but other assemblages would not be present if not for the primary hydrothermal mineralization. Low-temperature designations for most of the assemblages refer to ambient temperatures as opposed to hydrothermal. B, C) Photographs showing examples of fluid-flow pathways over short distances. Sample APDI-13-14b was collected within (B), and sample APDI-13-14a was collected within (C). In (C), the area outlined in light brown is marcasite with oxidized coatings (intermediates in A). Locations of these photos within the outcrop are shown in Fig. 5A.

have formed through alteration by sulfate-bearing fluids that resulted from interactions between the mixed sulfates and red coatings, the calcite host rock, and silicates within the impact melt rock. The 18.5 wt% SiO_2 in the sample and the identification of clays and microcline suggest a large contribution from the surrounding impact melt rocks, and this lithology may be a weathered clast of the silicate-bearing basement gneiss that is common in the impact melt rock (e.g., Osinski and Spray 2001).

The trends in weathering at this site as evidenced from the imaging spectroscopy measurements are similar to reported reactions that have been documented, albeit on much larger scales, at gossans and sites of acid mine drainage (e.g., Bigham and Nordstrom 2000; Jambor et al. 2000; Nordstrom et al. 2000). For example, airborne imaging spectroscopy has mapped mine sites with zones of sulfate and oxide mineralogies resulting from progressive neutralization of acid with increasing distance from the source (Swayze et al. 2000; Roach et al. 2006). These studies map more mature weathering products (i.e., jarosite, goethite, and hematite) than the main units at our site, where weathering products likely are less mature due to the low water–rock ratios and low weathering intensity in this polar desert. The vug studied here also differs from sites of acid mine drainage in that this calcite- and marcasite-bearing vug was formed in an impact-generated hydrothermal system (Osinski et al. 2001, 2005a).

Implications for Mars

This work has implications for understanding similar mineralogies and aqueous environments in

planetary exploration. While the vug itself is encased within clast-rich impact melt rocks and is not clearly visible from orbit, gypsum has been detected in orbital spectroscopic datasets covering the outcrop (Tornabene et al. 2005, 2014). This and other outcrops with gypsum signatures identified from orbit are thus promising sites for further exploration with field and ground investigations. The orbital detection of gypsum suggests that there was significant available sulfur for a hydrothermal system, should one develop. While this site is not a perfect analog for known deposits on Mars and massive carbonates as are present here have not been found on Mars (e.g., Edwards and Ehlmann 2015), the lithologies present at this vug are similar to some minerals detected on Mars. Sulfate-bearing units have been identified on Mars from orbital spectroscopy (e.g., Gendrin et al. 2005; Langevin et al. 2005; Bibring et al. 2006, 2007; Mustard et al. 2008; Bishop et al. 2009) and in situ rover measurements (e.g., Squyres et al. 2004a, 2004b, 2009; Vaniman et al. 2014), and there have been limited identifications of carbonates in situ (Boynton et al. 2009; Morris et al. 2010) and from orbit (e.g., Bandfield et al. 2003; Ehlmann et al. 2008). One lesson learned from our investigations is that a large portion of the outcrop today is dominated spectrally by sulfates and oxides that formed at ambient temperatures despite the deposit's origin in the impact-driven hydrothermal system. Similar processes could have occurred on Mars. Detection of sulfates that typically form at low temperatures on Mars does not preclude the existence of higher temperature aqueous conditions previously; the sulfates could have formed through oxidation and weathering of sulfides that formed at higher temperatures. This formation mechanism is particularly relevant where sulfates are identified near a source of heat, such as within an impact structure or in volcanic terrains. In addition, we note that, while this outcrop is volumetrically dominated by carbonates, coatings of iron sulfates, sulfides, and oxyhydroxides dominate the spectral signatures at the outcrop scale and mask signatures of the carbonates. Similar relationships could be present on Mars. The polar desert environment in the High Arctic where the Haughton impact structure is located is a good analog for the current climate of Mars, and the types of weathering seen here may well have occurred on Mars.

In addition, this site is relevant to astrobiological investigations of Mars. The existence of an active hydrothermal system postimpact led to present-day deposits of both oxidized and reduced assemblages that provide a redox gradient that can be exploited by microorganisms, as discussed in detail by Izawa et al. (2011). Previously, sulfur isotopic fractionations measured within the marcasite of the vug indicate active biotic processes temporal with the formation of the sulfides (Parnell et al. 2010); the later low-temperature weathering processes may have also had microbial components (Izawa et al. 2011). In acid mine drainage sites with similar mineralogies, microbes are often present and can significantly increase rates of iron and sulfur oxidation (e.g., Nordstrom and Southam 1997; Al et al. 2000; Schippers et al. 2010), and Izawa et al. (2011) suggested that similar iron and sulfur oxidizers could be present at this site. Our map (Fig. 5) extends the work of Izawa et al. (2011) by mapping the locations of these redox and chemical gradients both within single assemblages and at the borders between different units where Izawa et al. (2011) suggested that microbes are most likely to be found. Based on our results (Fig. 5), Fe^{2+} within the marcasite, on the boundaries between the marcasite and oxidized coatings of jarosite and gypsum, and in the popcorn-textured phase of copiapite, fibroferrite, gypsum, and melanterite could all host iron-oxidizing communities. Sulfur oxidizers might be expected at boundaries between marcasite and sulfate-bearing assemblages, while acidophiles could be present in fluids with low pH values such as are typically needed to form copiapite. Examples of boundaries where redox gradients are present are shown at higher resolution in photographs in Fig. 6; in particular, boundaries between the marcasite and oxidized marcasite as well as between the mixed sulfates and red coating would be promising locations to search for evidence of microbial activity. Finally, there is potential for preservation of thermophiles or hyperthermophiles within the marcasite in the vug if present during formation of the marcasite from hydrothermal fluids (Izawa et al. 2011). The imaging spectroscopy technique utilized here allows for the remote assessment of the mineralogies present, revealing areas of potential biological interest and helping to identify ideal sampling locations for planetary exploration missions. Future work aims at exploring the putative biology associated with these deposits and will strive to elucidate whether or not microbial activity correlates with the redox boundaries defined in this study.

Finally, this study also serves in part as a proof-of-concept for the utility of imaging spectroscopy in determining mineralogy, past aqueous conditions, and astrobiological potential in planetary exploration. The spectral techniques used here are validated by laboratory measurements and provide new insights into the weathering processes at this vug. Spectral parameters are commonly used to highlight spectral variance in imaging spectroscopy data (e.g., Pelkey et al. 2007; Viviano-Beck et al. 2014) to aid in detecting minerals and mapping lithologies. Spectral parameters

mapping slopes or depths of single absorption features are nonunique in that a spectral feature at a given wavelength often is present in more than one mineral or the cause of a spectral slope may be due to many factors. To make parameters more reliable, we developed mineral and lithologic indicator parameters to detect the presence (and absence) of specific absorption features characteristic of minerals of interest. By combining spectral parameters, more robust mineral detections and mineral assemblage determinations are possible (e.g., Viviano-Beck et al. 2014). Validation of the accuracy of a particular parameter or suite of parameters for mineral detection is typically approached by detailed spectral analysis of a subset of the highlighted pixels to assess the rate of false positives. Samples from key sites detected in the remotely sensed data are also analyzed using other laboratory or in situ methods to increase confidence in the mapping. The parameters used in this work were finely tuned to the particular lithologies present at this outcrop, making the rate of false positives quite low.

Imaging spectroscopy is a powerful tool both to obtain an initial assessment of what compositional units are present and where there is variability and to scale more limited and costly targeted laboratory analyses to larger samples and outcrops (Greenberger et al. 2015b). Our results here show the evolution from a reducing hydrothermal system to low-temperature fluids that become progressively more oxidizing, evolve from acidic to more neutral, and change from simpler chemistries dominated by Fe and sulfate to more complex solutions incorporating Ca after reacting with the calcite host rock. With an imaging spectrometer extending into the shortwave infrared similar to the SWIR imager used in the laboratory, mineralogies at the outcrop could be mapped directly by the overtones and combination tones of vibrational absorption features, providing additional constraints on the precise mineralogies present, the past aqueous environments, and the habitability at this outcrop or on Mars.

CONCLUSIONS

Hydrothermal systems generated by meteorite impacts are likely to be important in the formation of secondary phases on both Earth and Mars and provide habitats for microbial colonization (e.g., Izawa et al. 2011; Sapers et al. 2014). This work investigated a hydrothermal calcite- and marcasite-bearing vug at the Haughton impact structure that has undergone low-temperature weathering using hyperspectral imaging in the field and laboratory as well as supporting reflectance spectroscopy, mineralogy, and chemistry measurements. The mineral assemblages identified and mapped at the outcrop are as follows: unaltered marcasite; oxidized marcasite with a coating of gypsum and jarosite; a mixed sulfate phase consisting of fibroferrite, copiapite, and minor gypsum and melanterite; a red coating of gypsum, akaganeite, goethite, and jarosite; and a blue-gray phase with calcite, gypsum, clays, microcline, quartz, and hematite.

The aqueous conditions that altered this outcrop have been inferred from the mineral assemblages. The marcasite likely formed at high temperatures during the postimpact hydrothermal system, and the other phases formed at ambient temperatures after the hydrothermal system cooled. The oxidized coatings on marcasite probably formed first in a system with low water/rock ratios that partially oxidized the Fe and S. Extremely acidic fluids that had interacted with the marcasite then likely dripped onto flatter surfaces below, resulting in precipitation of the fibroferrite and copiapite/ferricopiapite mixed sulfate phase. We argue that those minerals then underwent some dissolution, and the resulting fluids interacted with the calcite host rock, dissolving some calcite while neutralizing the acidic fluids somewhat, leading to precipitation of gypsum and Fe^{3+}-oxide/sulfate-bearing coatings. The spectral units mapped and the inferred changes in fluid chemistry and oxidation state with progressive alteration are relevant to Mars and can be used to predict the locations of microbial populations, with biosignatures most likely to be found at boundaries between various mapped units. This study also shows the utility of hyperspectral imaging in exploring sites that have undergone aqueous alteration, including through impact-driven processes, and in assessing their astrobiological potential on another planet.

Acknowledgments—We thank Paul Mann for his efforts in maintaining, packing, and shipping the equipment that made this work possible and David Bannon, Kwok Wong, and Headwall Photonics, Inc. for use of their hyperspectral imagers in the laboratory. We thank Dave Murray and Joe Orchardo for assistance with flux fusion, ICP-AES, and elemental analyses. We are also grateful for help in the field from other members of the field team: Jerome Gattacceca, Jeremy Hansen, Yoann Quesnel, Pierre Rochette, and Scott Simpson. We thank Brown University for supporting this research. The Polar Continental Shelf Program provided field support for this work. Funding from the Natural Sciences and Engineering Research Council (NSERC) Discovery Grant and Northern Supplement program funded GRO, LLT, AP, and CLM. AP and CLM also thank the Northern Scientific Training Program for funding. EAC thanks the University of Winnipeg, the Canadian Space Agency, the Manitoba Research Innovations

Funds, and NSERC of Canada for supporting the establishment of the University of Winnipeg's Planetary Spectrophotometer Facility and this study. Finally, we thank Carle Pieters for editorial handling and Adrian Brown and Matthew Izawa for constructive reviews that significantly improved this paper. The authors confirm that there is no conflict of interest to declare.

Editorial Handling—Dr. Carle Pieters

REFERENCES

Abramov O. and Kring D. A. 2005. Impact-induced hydrothermal activity on early Mars. *Journal of Geophysical Research* 110:E12S09.

Aines R. D. and Rossman G. R. 1984. Water in minerals? A peak in the infrared. *Journal of Geophysical Research: Solid Earth* 89:4059–4071.

Al T. A., Martin C. J., and Blowes D. W. 2000. Carbonate-mineral/water interactions in sulfide-rich mine tailings. *Geochimica et Cosmochimica Acta* 64:3933–3948.

Arvidson R. E., Squyres S. W., Bell J. F., Catalano J. G., Clark B. C., Crumpler L. S., de Souza P. A., Fairén A. G., Farrand W. H., Fox V. K., Gellert R., Ghosh A., Golombek M. P., Grotzinger J. P., Guinness E. A., Herkenhoff K. E., Jolliff B. L., Knoll A. H., Li R., McLennan S. M., Ming D. W., Mittlefehldt D. W., Moore J. M., Morris R. V., Murchie S. L., Parker T. J., Paulsen G., Rice J. W., Ruff S. W., Smith M. D., and Wolff M. J. 2014. Ancient aqueous environments at Endeavour Crater. *Mars. Science* 343:1248097.

Bandfield J. L., Glotch T. D., and Christensen P. R. 2003. Spectroscopic identification of carbonate minerals in the Martian dust. *Science* 301:1084–1087.

Bibi I., Singh B., and Silvester E. 2011. Akaganéite (β-FeOOH) precipitation in inland acid sulfate soils of south-western New South Wales (NSW), Australia. *Geochimica et Cosmochimica Acta* 75:6429–6438.

Bibring J.-P., Langevin Y., Mustard J. F., Poulet F., Arvidson R., Gendrin A., Gondet B., Mangold N., Pinet P., Forget F., and the OMEGA team. 2006. Global mineralogical and aqueous Mars history derived from OMEGA/Mars Express data. *Science* 312:400–404.

Bibring J.-P., Arvidson R. E., Gendrin A., Gondet B., Langevin Y., Mouelic S. L., Mangold N., Morris R. V., Mustard J. F., Poulet F., Quantin C., and Sotin C. 2007. Coupled ferric oxides and sulfates on the Martian surface. *Science* 317:1206–1210.

Bigham J. M. and Nordstrom D. K. 2000. Iron and aluminum hydroxysulfates from acid sulfate waters. *Reviews in Mineralogy and Geochemistry* 40:351–403.

Bishop J. L., Parente M., Weitz C. M., Noe Dobrea E. Z., Roach L. H., Murchie S. L., McGuire P. C., McKeown N. K., Rossi C. M., Brown A. J., Calvin W. M., Milliken R., and Mustard J. F. 2009. Mineralogy of Juventae Chasma: Sulfates in the light-toned mounds, mafic minerals in the bedrock, and hydrated silica and hydroxylated ferric sulfate on the plateau. *Journal of Geophysical Research: Planets* 114:E00D09.

Booth J., Hong Q., Compton R. G., Prout K., and Payne R. M. 1997. Gypsum overgrowths passivate calcite to acid attack. *Journal of Colloid and Interface Science* 192:207–214.

Boynton W. V., Ming D. W., Kounaves S. P., Young S. M. M., Arvidson R. E., Hecht M. H., Hoffman J., Niles P. B., Hamara D. K., Quinn R. C., Smith P. H., Sutter B., Catling D. C., and Morris R. V. 2009. Evidence for calcium carbonate at the Mars Phoenix landing site. *Science* 325:61–64.

Brown A. J. 2014. Spectral bluing induced by small particles under the Mie and Rayleigh regimes. *Icarus* 239:85–95.

Burns R. G. 1993. *Mineralogical applications of crystal field theory*, 2nd ed. Cambridge, UK: Cambridge University Press. 551 p.

Chavez P. S. 1988. An improved dark-object subtraction technique for atmospheric scattering correction of multispectral data. *Remote Sensing of Environment* 24:459–479.

Chavez P. S. 1996. Image-based atmospheric corrections-revisited and improved. *Photogrammetric Engineering & Remote Sensing* 62:1025–1036.

Chou I.-M., Seal R. R. II, and Wang A. 2013. The stability of sulfate and hydrated sulfate minerals near ambient conditions and their significance in environmental and planetary sciences. *Journal of Asian Earth Sciences* 62:734–758.

Clark R. N. and Roush T. L. 1984. Reflectance spectroscopy: Quantitative analysis techniques for remote sensing applications. *Journal of Geophysical Research* 89:6329–6340.

Clark R. N., King T. V. V., Klejwa M., Swayze G. A., and Vergo N. 1990. High spectral resolution reflectance spectroscopy of minerals. *Journal of Geophysical Research* 95:12653–12680.

Clark R. N., Swayze G. A., Livo K. E., Kokaly R. F., King T. V. V., Dalton J. B., Vance J. S., Rockwell B. W., Hoefen T., and McDougal R. R. 2002. Surface reflectance calibration of terrestrial imaging spectroscopy data: A tutorial using AVIRIS. *Proceedings, 10th Airborne Earth Science Workshop*. pp. 02–1.

Clark R. N., Swayze G. A., Wise R., Livo E., Hoefen T., Kokaly R., and Sutley S. J. 2007. USGS digital spectral library splib06a. U.S. Geological Survey, Digital Data Series 231. Washington, DC: U.S. Department of the Interior.

Clark R. N., Curchin J. M., Jaumann R., Cruikshank D. P., Brown R. H., Hoefen T. M., Stephan K., Moore J. M., Buratti B. J., Baines K. H., Nicholson P. D., and Nelson R. M. 2008. Compositional mapping of Saturn's satellite Dione with Cassini VIMS and implications of dark material in the Saturn system. *Icarus* 193:372–386.

Cloutis E. A. and Gaffey M. J. 1994. An X-ray diffraction and reflectance spectroscopy study of iron sulphides. Proceedings, 25th Lunar and Planetary Science Conference. pp. 273–274.

Cloutis E. A., Hawthorne F. C., Mertzman S. A., Krenn K., Craig M. A., Marcino D., Methot M., Strong J., Mustard J. F., Blaney D. L., Bell J. F. III, and Vilas F. 2006. Detection and discrimination of sulfate minerals using reflectance spectroscopy. *Icarus* 184:121–157.

Crowley J. K., Williams D. E., Hammarstrom J. M., Piatak N., Chou I.-M., and Mars J. C. 2003. Spectral reflectance properties (0.4–2.5 μm) of secondary Fe-oxide, Fe-hydroxide, and Fe-sulphate-hydrate minerals associated with sulphide-bearing mine wastes. *Geochemistry: Exploration, Environment, Analysis* 3:219–228.

Cull-Hearth S., van Venrooy A., Clark M. C., and Cvitkovic A. 2016. Acid-sulfate mixtures from Río Tinto, Spain: Spectral masking relationships and implications for Mars. *Icarus* 271:387–399.

Edwards C. S. and Ehlmann B. L. 2015. Carbon sequestration on Mars. *Geology* 43:863–866.

Ehlmann B. L., Mustard J. F., Murchie S. L., Poulet F., Bishop J. L., Brown A. J., Calvin W. M., Clark R. N., Marais D. J. D., Milliken R. E., Roach L. H., Roush T. L., Swayze G. A., and Wray J. J. 2008. Orbital identification of carbonate-bearing rocks on Mars. *Science* 322:1828–1832.

Elwood Madden M. E., Bodnar R. J., and Rimstidt J. D. 2004. Jarosite as an indicator of water-limited chemical weathering on Mars. *Nature* 431:821–823.

Fischer E. M. and Pieters C. M. 1993. The continuum slope of Mars: Bidirectional reflectance investigations and applications to Olympus Mons. *Icarus* 102:185–202.

Flemming R. L. 2007. Micro X-ray diffraction (μXRD): A versatile technique for characterization of Earth and planetary materials. *Canadian Journal of Earth Sciences* 44:1333–1346.

Gendrin A., Mangold N., Bibring J.-P., Langevin Y., Gondet B., Poulet F., Bonello G., Quantin C., Mustard J., Arvidson R., and LeMouélic S. 2005. Sulfates in Martian layered terrains: The OMEGA/Mars Express view. *Science* 307:1587–1591.

Goryniuk M. C., Rivard B. A., and Jones B. 2004. The reflectance spectra of opal-A (0.5–25 μm) from the Taupo Volcanic Zone: Spectra that may identify hydrothermal systems on planetary surfaces. *Geophysical Research Letters* 31:L24701.

Greenberger R. N., Mustard J. F., Cloutis E. A., Mann P., Wilson J. H., Flemming R. L., Robertson K. M., Salvatore M. R., and Edwards C. S. 2015a. Hydrothermal alteration and diagenesis of terrestrial lacustrine pillow basalts: Coordination of hyperspectral imaging with laboratory measurements. *Geochimica Cosmochimica Acta* 171:174–200.

Greenberger R. N., Mustard J. F., Ehlmann B. L., Blaney D. L., Cloutis E. A., Wilson J. H., Green R. O., and Fraeman A. A. 2015b. Imaging spectroscopy of geological samples and outcrops: Novel insights from microns to meters. *GSA Today* 25:4–10.

Hagerty J. J. and Newsom H. E. 2003. Hydrothermal alteration at the Lonar Lake impact structure, India: Implications for impact cratering on Mars. *Meteoritics & Planetary Science* 38:365–381.

Hunt G. R. and Salisbury J. W. 1971. Visible and near infrared spectra of minerals and rocks. II. Carbonates. *Modern Geology* 2:23–30.

Hunt G. R., Salisbury J. W., and Lenhoff C. J. 1971. Visible and near-infrared spectra of minerals and rocks. IV. Sulphides and sulphates. *Modern Geology* 3:1–14.

Izawa M. R. M., Banerjee N. R., Osinski G. R., Flemming R. L., Parnell J., and Cockell C. S. 2011. Weathering of post-impact hydrothermal deposits from the Haughton impact structure: Implications for microbial colonization and biosignature preservation. *Astrobiology* 11:537–550.

Jambor J. L., Nordstrom D. K., and Alpers C. N. 2000. Metal-sulfate salts from sulfide mineral oxidation. *Reviews in Mineralogy and Geochemistry* 40:303–350.

Jamieson H. E., Robinson C., Alpers C. N., McCleskey R. B., Nordstrom D. K., and Peterson R. C. 2005. Major and trace element composition of copiapite-group minerals and coexisting water from the Richmond mine, Iron Mountain, California. *Chemical Geology* 215:387–405.

Johnson J. R. and Grundy W. M. 2001. Visible/near-infrared spectra and two-layer modeling of palagonite-coated basalts. *Geophysical Research Letters* 28:2101–2104.

Kring D. A. 2000. Impact events and their effect on the origin, evolution, and distribution of life. *GSA Today* 10:1–7.

Langevin Y., Poulet F., Bibring J.-P., and Gondet B. 2005. Sulfates in the north polar region of Mars detected by OMEGA/Mars Express. *Science* 307:1584–1586.

Lindsay M. B. J., Moncur M. C., Bain J. G., Jambor J. L., Ptacek C. J., and Blowes D. W. 2015. Geochemical and mineralogical aspects of sulfide mine tailings. *Applied Geochemistry* 57:157–177.

Marzo G. A., Davila A. F., Tornabene L. L., Dohm J. M., Fairén A. G., Gross C., Kneissl T., Bishop J. L., Roush T. L., and McKay C. P. 2010. Evidence for Hesperian impact-induced hydrothermalism on Mars. *Icarus* 208:667–683.

Morris R. V., Ruff S. W., Gellert R., Ming D. W., Arvidson R. E., Clark B. C., Golden D. C., Siebach K., Klingelhöfer G., Schröder C., Fleischer I., Yen A. S., and Squyres S. W. 2010. Identification of carbonate-rich outcrops on Mars by the Spirit Rover. *Science* 329:421–424.

Murray R., Miller D. J., and Kryc K. 2000. Analysis of major and trace elements in rocks, sediments, and interstitial waters by inductively coupled plasma–atomic emission spectrometry (ICP-AES). *ODP Technical Note* 29:1–27.

Mustard J. F., Murchie S. L., Pelkey S. M., Ehlmann B. L., Milliken R. E., Grant J. A., Bibring J.-P., Poulet F., Bishop J., Dobrea E. N., Roach L., Seelos F., Arvidson R. E., Wiseman S., Green R., Hash C., Humm D., Malaret E., McGovern J. A., Seelos K., Clancy T., Clark R., Marais D. D., Izenberg N., Knudson A., Langevin Y., Martin T., McGuire P., Morris R., Robinson M., Roush T., Smith M., Swayze G., Taylor H., Titus T., and Wolff M. 2008. Hydrated silicate minerals on Mars observed by the Mars Reconnaissance Orbiter CRISM instrument. *Nature* 454:305–309.

Naumov M. V. 2005. Principal features of impact-generated hydrothermal circulation systems: Mineralogical and geochemical evidence. *Geofluids* 5:165–184. doi:10.1111/j.1468-8123.2005.00092.x.

Newsom H. E. 1980. Hydrothermal alteration of impact melt sheets with implications for Mars. *Icarus* 44:207–216.

Newsom H. E., Brittelle G. E., Hibbitts C. A., Crossey L. J., and Kudo A. M. 1996. Impact crater lakes on Mars. *Journal of Geophysical Research: Planets* 101:14,951–14,955.

Newsom H. E., Hagerty J. J., and Thorsos I. E. 2001. Location and sampling of aqueous and hydrothermal deposits in Martian impact craters. *Astrobiology* 1:71–88.

Nordstrom D. K. and Southam G. 1997. Geomicrobiology of sulfide mineral oxidation. *Reviews in Mineralogy and Geochemistry* 35:361–390.

Nordstrom D. K., Alpers C. N., Ptacek C. J., and Blowes D. W. 2000. Negative pH and extremely acidic mine waters from Iron Mountain, California. *Environmental Science and Technology* 34:254–258.

Osinski G. R. and Spray J. G. 2001. Impact-generated carbonate melts: Evidence from the Haughton structure, Canada. *Earth and Planetary Science Letters* 194:17–29.

Osinski G. R. and Spray J. G. 2003. Evidence for the shock melting of sulfates from the Haughton impact structure,

Arctic Canada. *Earth and Planetary Science Letters* 215:357–370.

Osinski G. R., Spray J. G., and Lee P. 2001. Impact-induced hydrothermal activity within the Haughton impact structure, arctic Canada: Generation of a transient, warm, wet oasis. *Meteoritics & Planetary Science* 36:731–745.

Osinski G. R., Lee P., Parnell J., Spray J. G., and Baron M. 2005a. A case study of impact-induced hydrothermal activity: The Haughton impact structure, Devon Island, Canadian High Arctic. *Meteoritics & Planetary Science* 40:1859–1877.

Osinski G. R., Lee P., Spray J. G., Parnell J., Lim D. S. S., Bunch T. E., Cockell C. S., and Glass B. 2005b. Geological overview and cratering model for the Haughton impact structure, Devon Island, Canadian High Arctic. *Meteoritics & Planetary Science* 40:1759–1776.

Osinski G. R., Tornabene L. L., Banerjee N. R., Cockell C. S., Flemming R., Izawa M. R. M., McCutcheon J., Parnell J., Preston L. J., Pickersgill A. E., Pontefract A., Sapers H. M., and Southam G. 2013. Impact-generated hydrothermal systems on Earth and Mars. *Icarus* 224:347–363.

Parnell J., Boyce A., Thackrey S., Muirhead D., Lindgren P., Mason C., Taylor C., Still J., Bowden S., Osinski G. R., and Lee P. 2010. Sulfur isotope signatures for rapid colonization of an impact crater by thermophilic microbes. *Geology* 38:271–274.

Parnell J., Boyce A. J., Osinski G. R., Izawa M. R. M., Banerjee N., Flemming R., and Lee P. 2012. Evidence for life in the isotopic analysis of surface sulphates in the Haughton impact structure, and potential application on Mars. *International Journal of Astrobiology* 11:93–101.

Pelkey S. M., Mustard J. F., Murchie S., Clancy R. T., Wolff M., Smith M., Milliken R., Bibring J.-P., Gendrin A., Poulet F., Langevin Y., and Gondet B. 2007. CRISM multispectral summary products: Parameterizing mineral diversity on Mars from reflectance. *Journal of Geophysical Research* 112:E08S14.

Pieters C. M. 1983. Strength of mineral absorption features in the transmitted component of near-infrared reflected light: First results from RELAB. *Journal of Geophysical Research* 88(B11):9534–9544.

Roach L. H., Mustard J., Gendrin A., Fernández-Remolar D., Amils R., and Amaral-Zettler L. 2006. Finding mineralogically interesting targets for exploration from spatially coarse visible and near IR spectra. *Earth and Planetary Science Letters* 252:201–214.

Sapers H. M., Osinski G. R., Banerjee N. R., and Preston L. J. 2014. Enigmatic tubular features in impact glass. *Geology* 42:471–474.

Scheinost A. C., Chavernas A., Barron V., and Torrent J. 1998. Use and limitations of second-derivative diffuse reflectance spectroscopy in the visible to near-infrared range to identify and quantify Fe oxide minerals in soils. *Clays and Clay Minerals* 46:528–536.

Schippers A., Breuker A., Blazejak A., Bosecker K., Kock D., and Wright T. L. 2010. The biogeochemistry and microbiology of sulfidic mine waste and bioleaching dumps and heaps, and novel Fe(II)-oxidizing bacteria. *Hydrometallurgy* 104:342–350.

Schulze-Makuch D., Dohm J. M., Fan C., Fairén A. G., Rodriguez J. A. P., Baker V. R., and Fink W. 2007. Exploration of hydrothermal targets on Mars. *Icarus* 189:308–324.

Schwenzer S. P. and Kring D. A. 2009. Impact-generated hydrothermal systems capable of forming phyllosilicates on Noachian Mars. *Geology* 37:1091–1094.

Schwenzer S. P. and Kring D. A. 2013. Alteration minerals in impact-generated hydrothermal systems—Exploring host rock variability. *Icarus* 226:487–496.

Schwenzer S. P., Abramov O., Allen C. C., Clifford S. M., Cockell C. S., Filiberto J., Kring D. A., Lasue J., McGovern P. J., Newsom H. E., Treiman A. H., Vaniman D. T., and Wiens R. C. 2012. Puncturing Mars: How impact craters interact with the Martian cryosphere. *Earth and Planetary Science Letters* 335–336:9–17.

Singer R. B. and Roush T. L. 1983. Spectral reflectance properties of particulate weathered coatings on rocks: Laboratory modeling and applicability to Mars (abstract). 14th Lunar and Planetary Science Conference. p. 708.

Squyres S. W., Arvidson R. E., Bell J. F., Brückner J., Cabrol N. A., Calvin W., Carr M. H., Christensen P. R., Clark B. C., Crumpler L., Marais D. J. D., d'Uston C., Economou T., Farmer J., Farrand W., Folkner W., Golombek M., Gorevan S., Grant J. A., Greeley R., Grotzinger J., Haskin L., Herkenhoff K. E., Hviid S., Johnson J., Klingelhöfer G., Knoll A. H., Landis G., Lemmon M., Li R., Madsen M. B., Malin M. C., McLennan S. M., McSween H. Y., Ming D. W., Moersch J., Morris R. V., Parker T., Rice J. W., Richter L., Rieder R., Sims M., Smith M., Smith P., Soderblom L. A., Sullivan R., Wänke H., Wdowiak T., Wolff M., and Yen A. 2004a. The Opportunity rover's Athena science investigation at Meridiani Planum, Mars. *Science* 306:1698–1703.

Squyres S. W., Grotzinger J. P., Arvidson R. E., Bell J. F., Calvin W., Christensen P. R., Clark B. C., Crisp J. A., Farrand W. H., Herkenhoff K. E., Johnson J. R., Klingelhöfer G., Knoll A. H., McLennan S. M., McSween H. Y., Morris R. V., Rice J. W., Rieder R., and Soderblom L. A. 2004b. In situ evidence for an ancient aqueous environment at Meridiani Planum, Mars. *Science* 306:1709–1714.

Squyres S. W., Knoll A. H., Arvidson R. E., Ashley J. W., Bell J. F., Calvin W. M., Christensen P. R., Clark B. C., Cohen B. A., de Souza P. A., Edgar L., Farrand W. H., Fleischer I., Gellert R., Golombek M. P., Grant J., Grotzinger J., Hayes A., Herkenhoff K. E., Johnson J. R., Jolliff B., Klingelhöfer G., Knudson A., Li R., McCoy T. J., McLennan S. M., Ming D. W., Mittlefehldt D. W., Morris R. V., Rice J. W., Schröder C., Sullivan R. J., Yen A., and Yingst R. A. 2009. Exploration of Victoria Crater by the Mars Rover Opportunity. *Science* 324:1058–1061.

Squyres S. W., Arvidson R. E., Bell J. F., Calef F., Clark B. C., Cohen B. A., Crumpler L. A., de Souza P. A., Farrand W. H., Gellert R., Grant J., Herkenhoff K. E., Hurowitz J. A., Johnson J. R., Jolliff B. L., Knoll A. H., Li R., McLennan S. M., Ming D. W., Mittlefehldt D. W., Parker T. J., Paulsen G., Rice M. S., Ruff S. W., Schröder C., Yen A. S., and Zacny K. 2012. Ancient impact and aqueous processes at Endeavour Crater, Mars. *Science* 336:570–576.

Swayze G. A., Smith K. S., Clark R. N., Sutley S. J., Pearson R. M., Vance J. S., Hageman P. L., Briggs P. H., Meier A. L., Singleton M. J., and Roth S. 2000. Using imaging spectroscopy to map acidic mine waste. *Environmental Science & Technology* 34:47–54.

Tornabene L. L., Moersch J. E., Osinski G. R., Lee P., and Wright S. P. 2005. Spaceborne visible and thermal infrared

lithologic mapping of impact-exposed subsurface lithologies at the Haughton impact structure, Devon Island, Canadian High Arctic: Applications to Mars. *Meteoritics & Planetary Science* 40:1835–1858.

Tornabene L. L., Osinski G. R., and McEwen A. S. 2009. Parautochthonous megabreccias and possible evidence of impact-induced hydrothermal alteration in Holden Crater, Mars (abstract #1766). 40th Lunar and Planetary Science Conference. CD-ROM.

Tornabene L. L., Osinski G. R., McEwen A. S., Wray J. J., Craig M. A., Sapers H. M., and Christensen P. R. 2013. An impact origin for hydrated silicates on Mars: A synthesis. *Journal of Geophysical Research: Planets* 118:994–1012.

Tornabene L. L., Osinski G. R., Greenberger R. N., Bishop J. L., Cloutis E. A., Marion C. L., Mustard J. F., Pontefract A., and Ramsey M. S. 2014. The pre-, syn- and post-impact origin of hydrated phases: A case study based on the remote sensing and ground-truth at the Haughton Impact Structure, Nunavut, Canada (abstract #2710). 45th Lunar and Planetary Science Conference. CD-ROM.

Vaniman D. T., Bish D. L., Ming D. W., Bristow T. F., Morris R. V., Blake D. F., Chipera S. J., Morrison S. M., Treiman A. H., Rampe E. B., Rice M., Achilles C. N., Grotzinger J. P., McLennan S. M., Williams J., Bell J. F., Newsom H. E., Downs R. T., Maurice S., Sarrazin P., Yen A. S., Morookian J. M., Farmer J. D., Stack K., Milliken R. E., Ehlmann B. L., Sumner D. Y., Berger G., Crisp J. A., Hurowitz J. A., Anderson R., Marais D. J. D., Stolper E. M., Edgett K. S., Gupta S., Spanovich N., and Team M. S. L. 2014. Mineralogy of a Mudstone at Yellowknife Bay, Gale Crater, Mars. *Science* 343: 1243480.

Vincent R. K. 1972. An ERTS multispectral scanner experiment for mapping iron compounds. Presented at the Proceedings of the Eighth International Symposium on Remote Sensing of Environment, Ann Arbor, Michigan.

Viviano-Beck C. E., Seelos F. P., Murchie S. L., Kahn E. G., Seelos K. D., Taylor H. W., Taylor K., Ehlmann B. L., Wisemann S. M., Mustard J. F., and Morgan M. F. 2014. Revised CRISM spectral parameters and summary products based on the currently detected mineral diversity on Mars. *Journal of Geophysical Research: Planets* 119:1403–1431.

Whitney D. L. and Evans B. W. 2010. Abbreviations for names of rock-forming minerals. *American Mineralogist* 95:185–187.

Young K. E., van Soest M. C., Hodges K. V., Watson E. B., Adams B. A., and Lee P. 2013. Impact thermochronology and the age of Haughton impact structure, Canada. *Geophysical Research Letters* 40:3836–3840.

SUPPORTING INFORMATION

Additional supporting information may be found in the online version of this article:

Table S1. Equations and interpretations of spectral and mineral indicator parameters for laboratory hyperspectral imaging data.

Table S2. Equations and interpretations for spectral and lithological indicator parameters for NIR field hyperspectral imaging data.